Supplementary Information (SI) for Materials Advances.
This journal is © The Royal Society of Chemistry 2024

SUPPLEMENTARY INFORMATION

WATER SORPTION STUDIES WITH MESOPOROUS MULTIVARIATE MONOLITHS BASED ON UiO-66

Linia Gedi Marazani,[1] Victoria Gascon-Perez,[2] Ayush Pathak,[3] Michele Tricarico,[4] Jin-Chong Tan,[4] Michael J. Zaworotko,[2] Andrew E. H. Wheatley,[3] Banothile C. E. Makhubela,[5] and Gift Mehlana[*1]

1. Department of Chemical Sciences, Faculty of Science and Technology, Midlands State University, P Bag 9055 Senga Road Gweru, Zimbabwe.
2. Bernal Institute, Department of Chemical Sciences, University of Limerick, Limerick, V94 T9PX, Republic of Ireland.
3. Yusuf Hamied Department of Chemistry, University of Cambridge, Lensfield Road, Cambridge, CB2 1EW, United Kingdom.
4. Department of Engineering Science, University of Oxford, Parks Road, Oxford, OX1 3PJ, United Kingdom.
5. Centre for Synthesis and Catalysis, Department of Chemical Sciences, Faculty of Science, University of Johannesburg, Auckland Park 2006, South Africa.

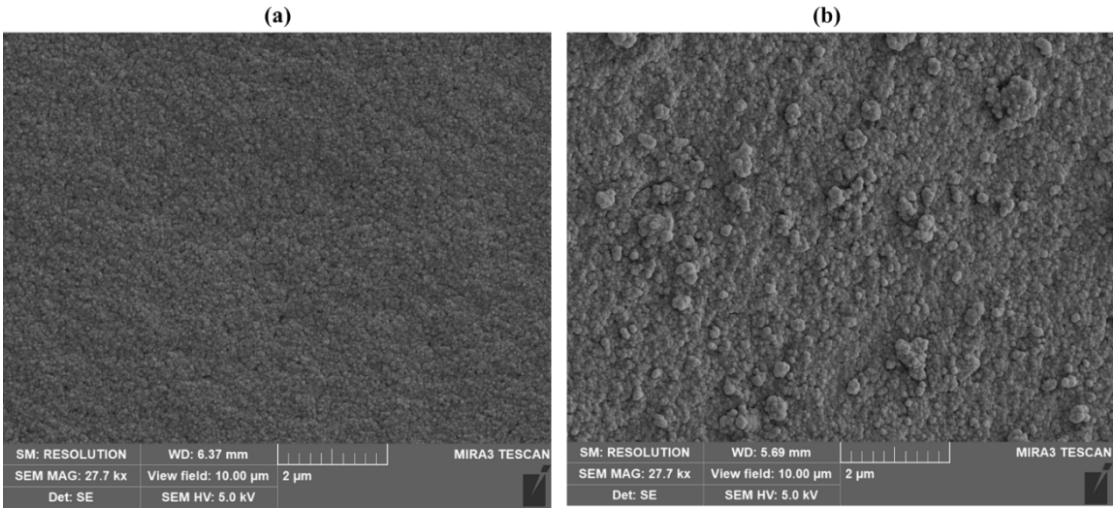

Figure S1: Representative SEM images for the monoliths (a) $_{mono}$UiO-66-NH_2-30%-B and (b) $_{mono}$UiO-66-NH_2-30%-A, contrasting the smoothness of the surface of the monolith before thermolysis (a) compared to after thermolysis (b).

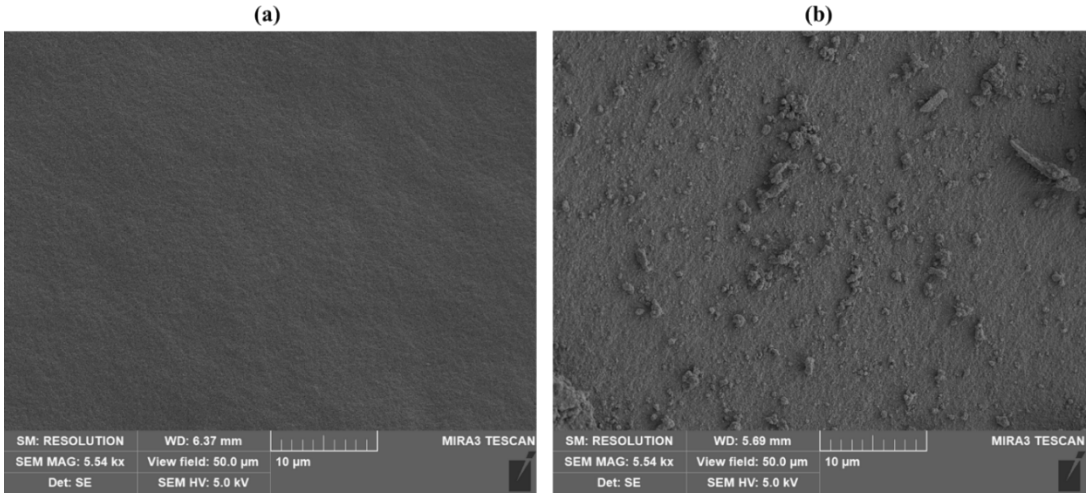

Figure S2: Representative low magnification SEM images for the monoliths (a) $_{mono}$UiO-66-NH_2-30%-B and (b) $_{mono}$UiO-66-NH_2-30%-A, contrasting the smoothness of the surface of the monolith before thermolysis (a) compared to after thermolysis (b).

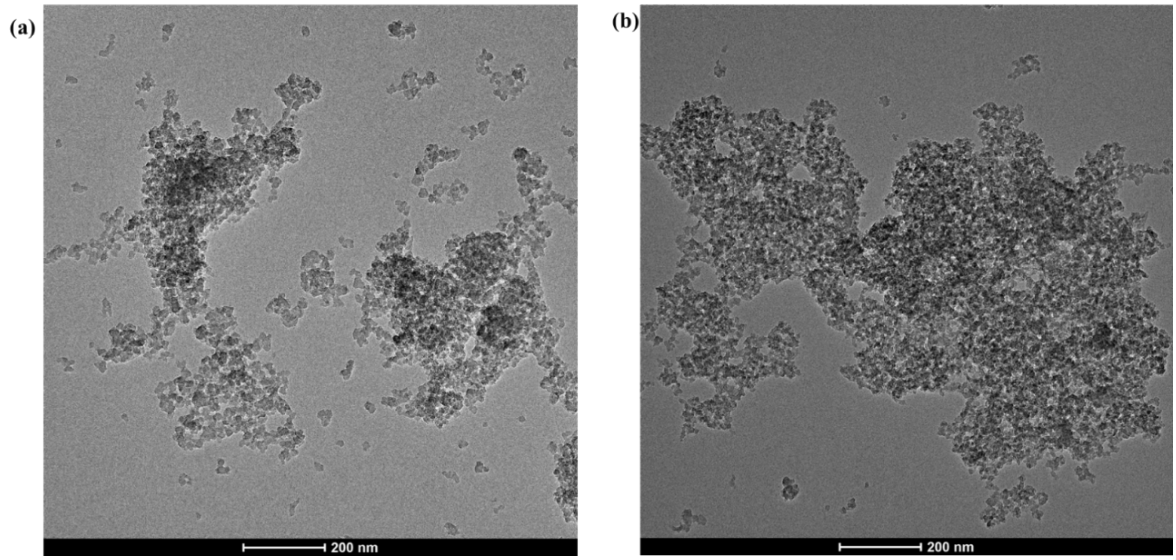

Figure S3: Representative low magnification TEM images of (a) $_{mono}$UiO-66-NH_2-30%-B and (b) $_{mono}$UiO-66-NH_2-30%-A.

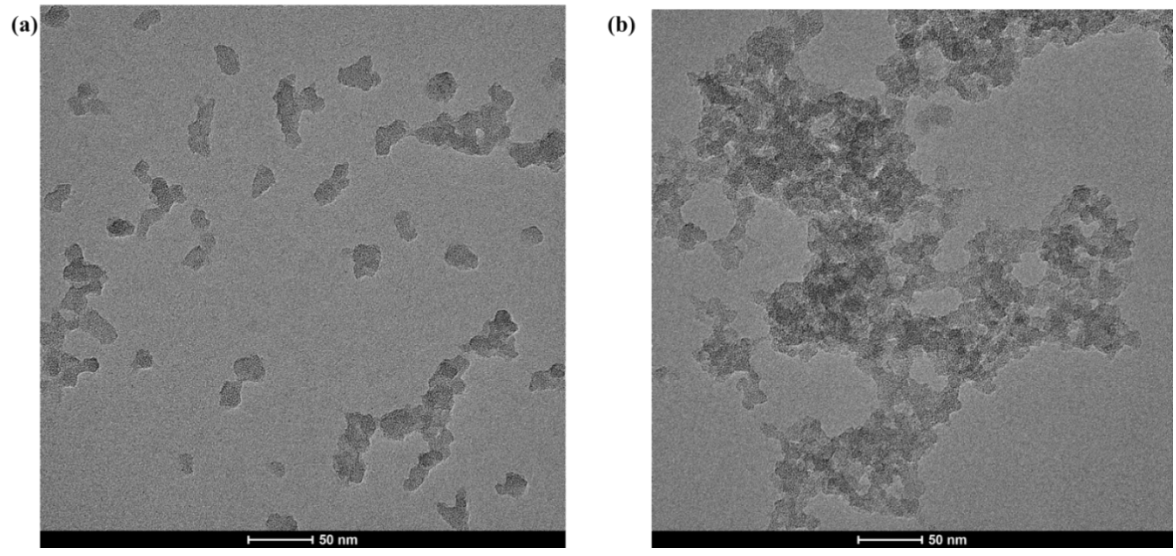

Figure S4: Representative TEM images of (a) $_{mono}$UiO-66-NH_2-30%-B and (b) $_{mono}$UiO-66-NH_2-30%-A.

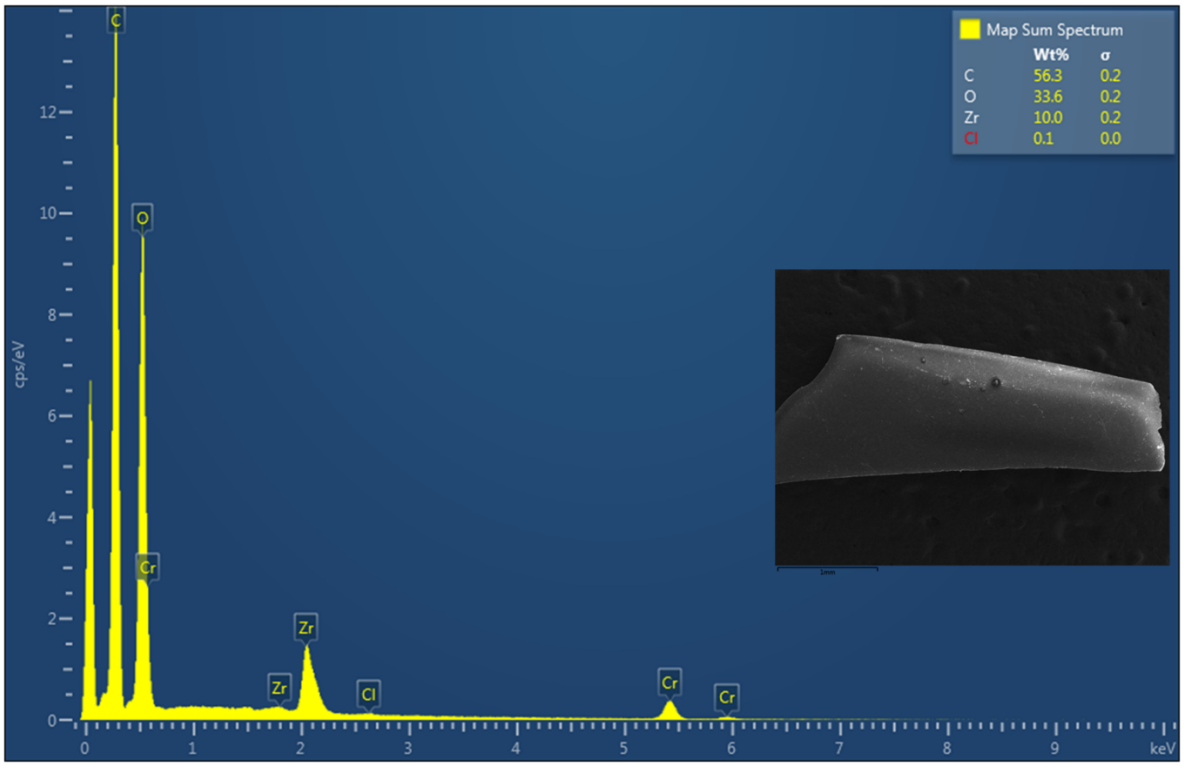

Figure S5: SEM-EDX plot for $_{mono}$UiO-66-NH_2-30%-B. Inset: Area scanned. The sample was sputter-coated with Cr for analysis.

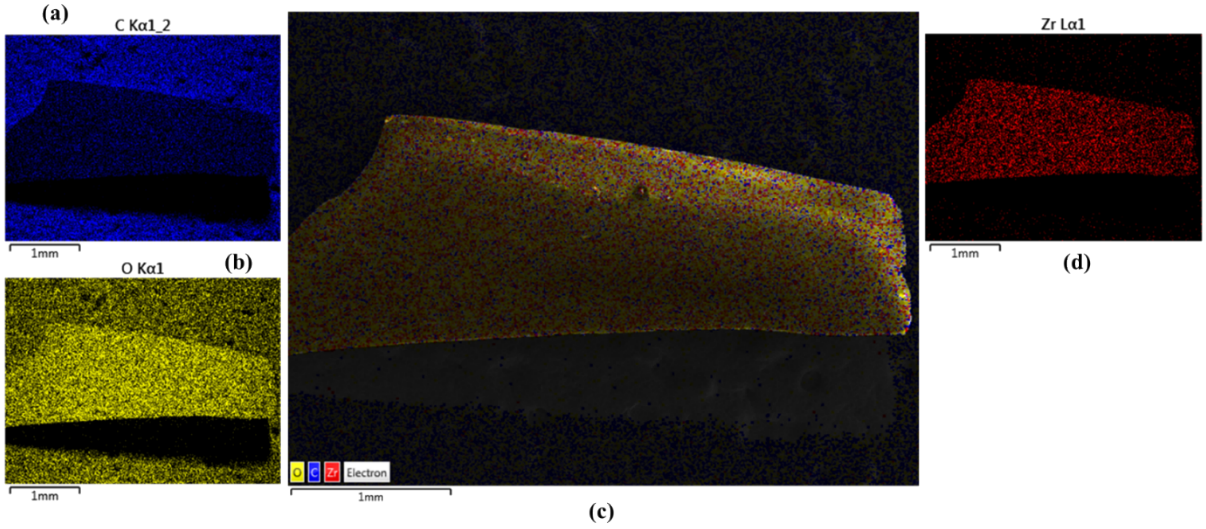

Figure S6: EDX elemental mapping showing how the elements are dispersed in $_{mono}$UiO-66-NH_2-30%-B: (a) carbon, (b) oxygen, (c) composite map, (d) zirconium. All the elements are evenly dispersed throughout the monolith, as shown in (c).

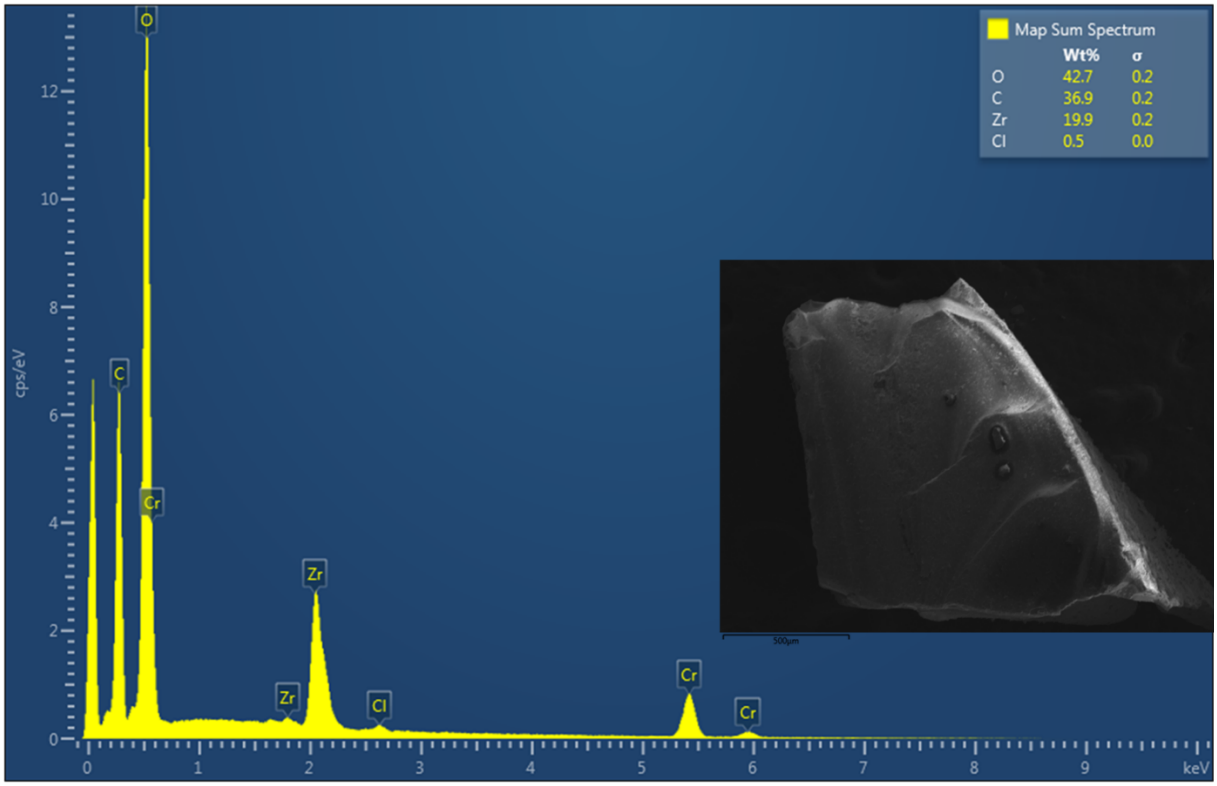

Figure S7: SEM-EDX plot for $_{mono}$UiO-66-NH_2-30%-A. Inset: Area scanned. The sample was sputter-coated with Cr for analysis.

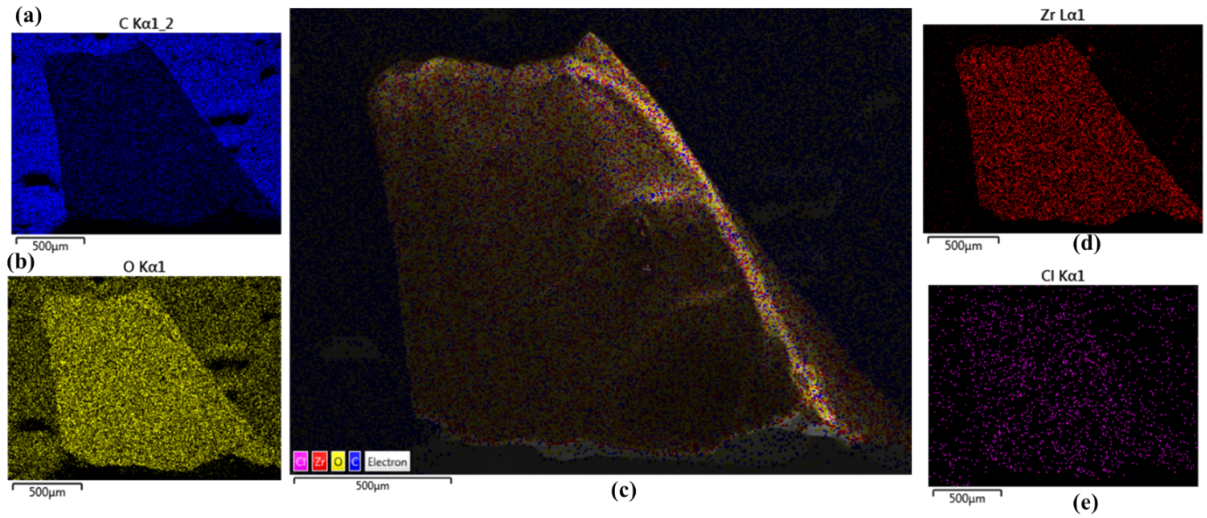

Figure S8: EDX elemental mapping showing how the elements are dispersed in $_{mono}$UiO-66-NH_2-30%-A: (a) carbon, (b) oxygen, (c) composite map, (d) zirconium, and (e) chlorine. All the elements are evenly dispersed throughout the monolith, as shown in (c).

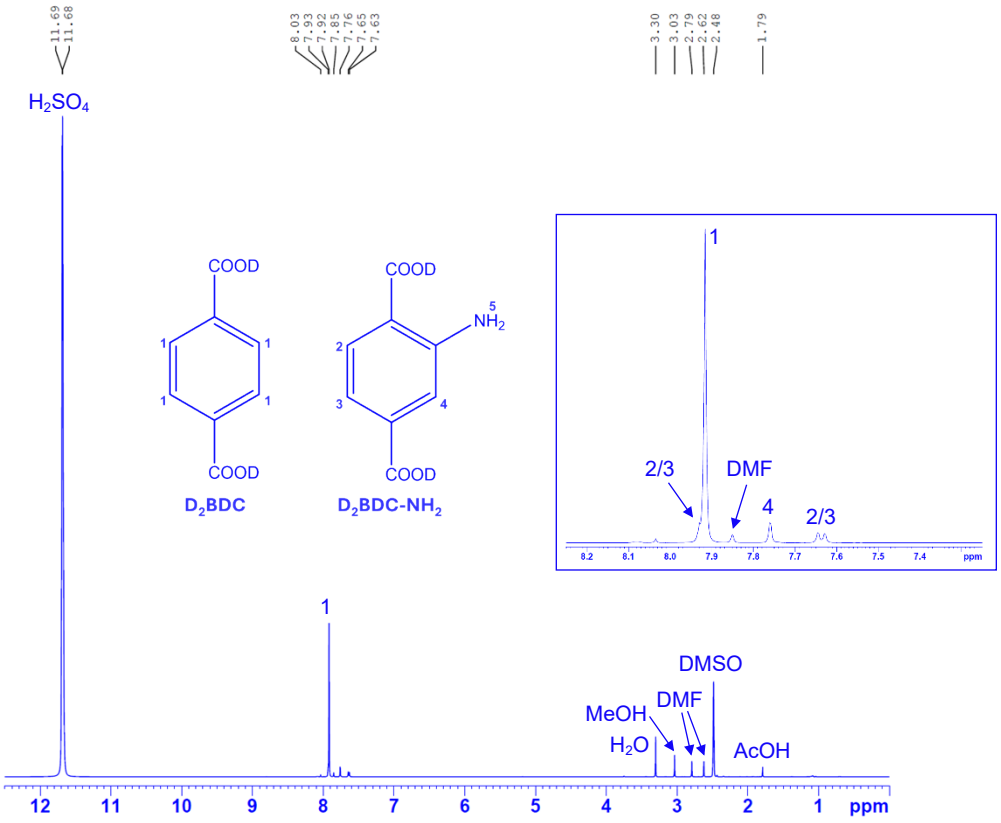

Figure S9: ^{1}H NMR spectrum of $_{mono}$UiO-66-NH_2-30%-B (500.200 MHz). Spectrum recorded at 27 °C, using DMSO-d_6 solvent after sample was initially digested in concentrated D_2SO_4. Inset: Expansion of the region δ 8.2-7.3 ppm.

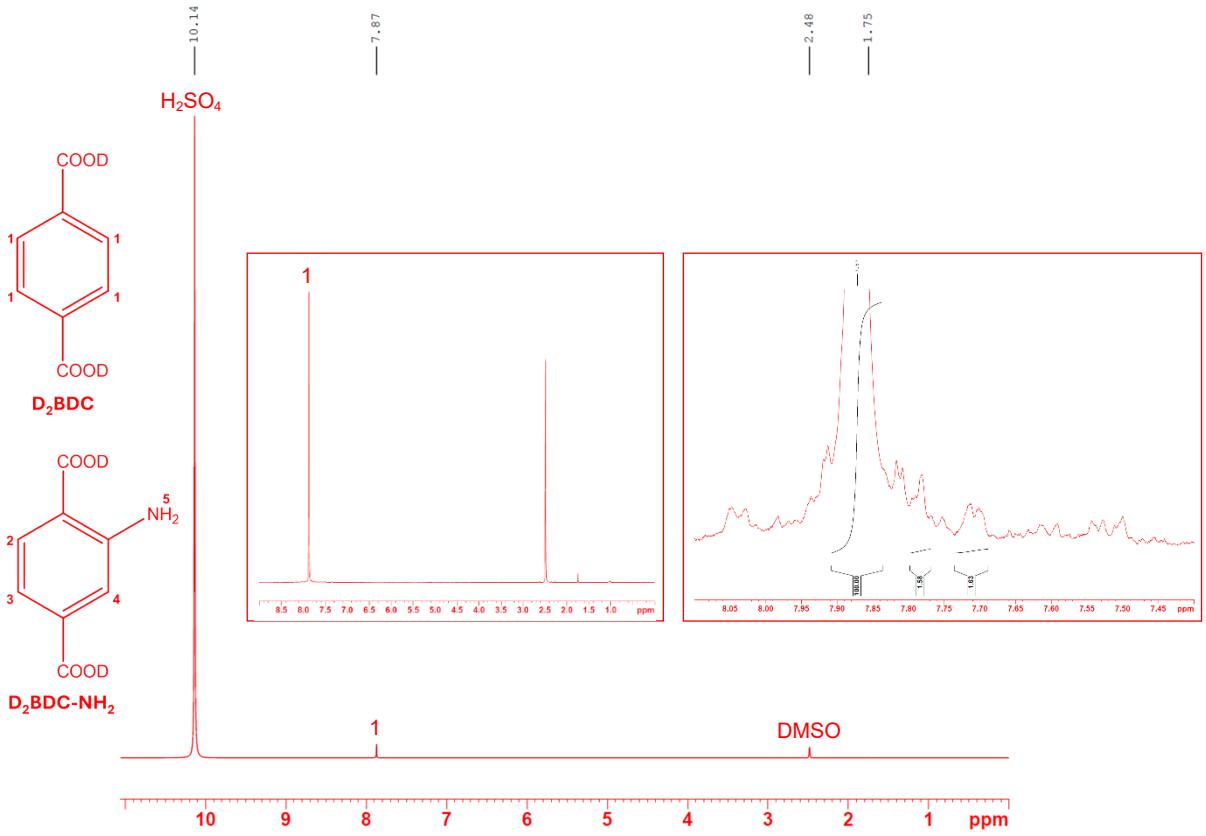

Figure S10: ^{1}H NMR spectrum of $_{mono}$UiO-66-NH_2-30%-A (500.200 MHz). Spectrum obtained at 27 °C, using DMSO-d_6 solvent after sample was initially digested in concentrated D_2SO_4. Inset left: Expansion of the region δ 8.5-0.0 ppm. Inset right: Expansion of the aromatic region suggesting non-zero levels of BDC-NH_2 after thermolabilization.

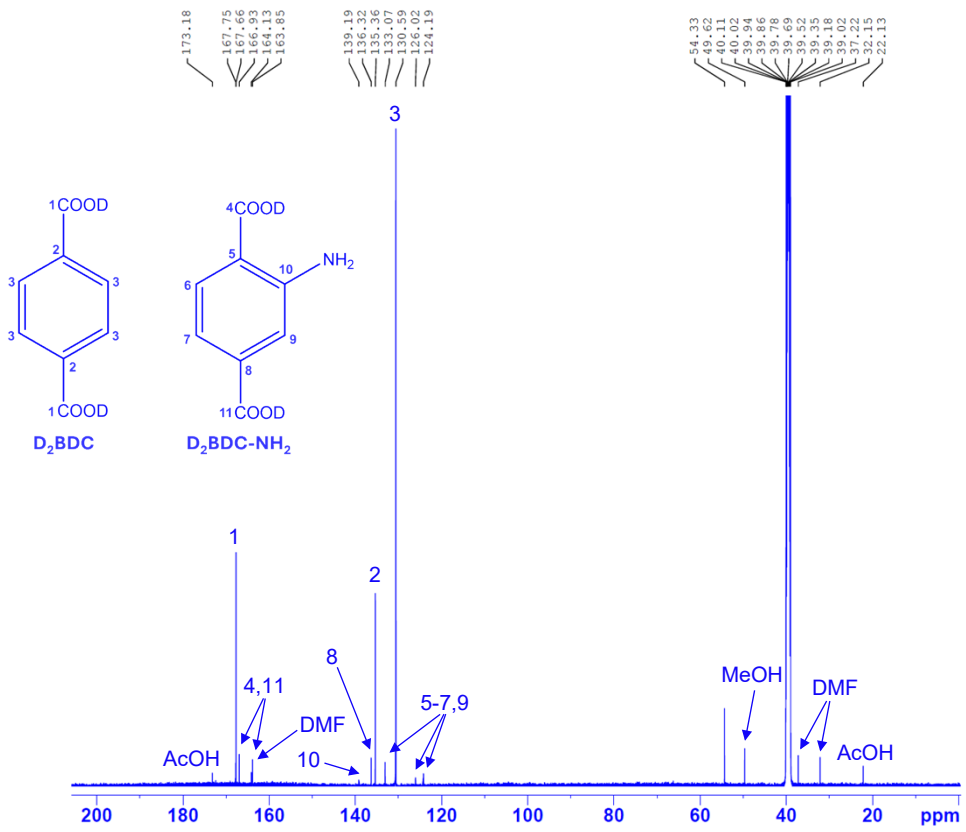

Figure S11: $^{13}C(^{1}H)$ NMR spectrum of $_{mono}$UiO-66-NH_2-30%-B (125.775 MHz). Spectrum obtained at 27 °C, using DMSO-d_6 solvent after sample was initially digested in concentrated D_2SO_4.

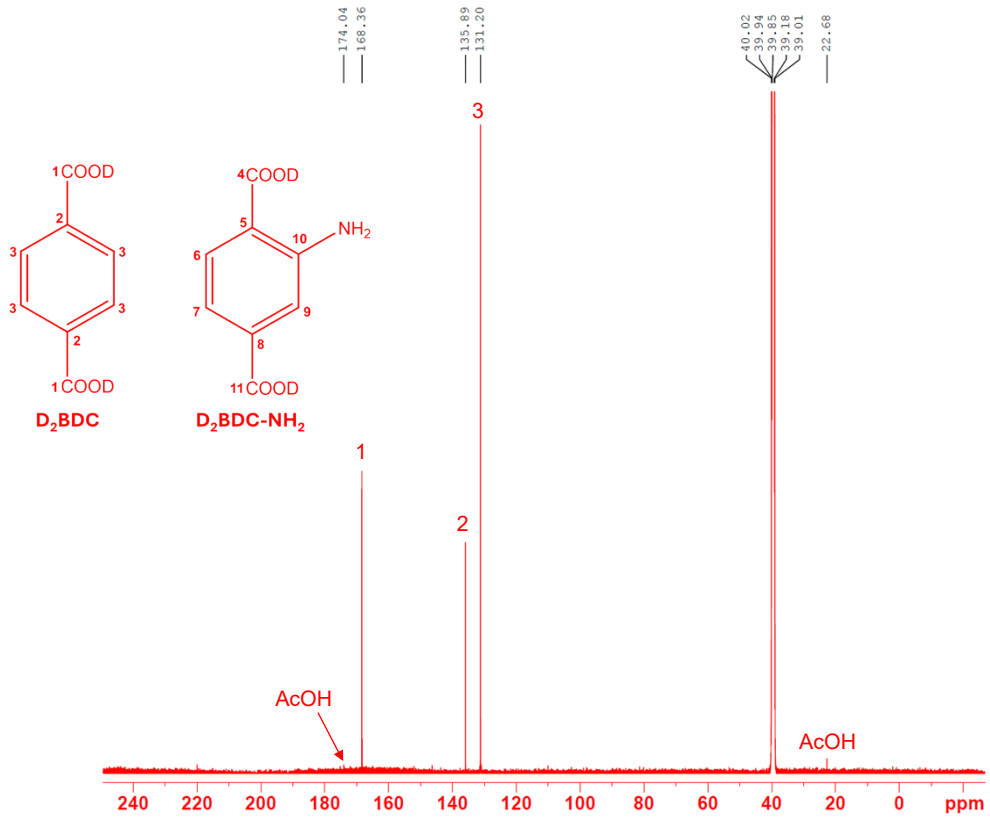

Figure S12: $^{13}C(^{1}H)$ NMR spectrum of $_{mono}$UiO-66-NH_2-30%-A (125.775 MHz). Spectrum obtained at 27 °C, using DMSO-d_6 solvent after sample was initially digested in concentrated D_2SO_4.

Figure S13: Stacked $^{13}C(^{1}H)$ NMR spectra of $_{mono}$UiO-66-NH_2-30%-B (blue) and $_{mono}$UiO-66-NH_2-30%-A (red) shown in Figures S11-S12.

Table S1: Nanoindentation data for $_{mono}$UiO-66-NH_2-30%-B and $_{mono}$UiO-66-NH_2-30%-A. The average values and standard deviations were determined from 32 measurements.

SAMPLE	MAX DEPTH (NM)	INDENTATION MODULUS (GPa)	HARDNESS (MPa)
$_{mono}$UiO-66-NH_2-30%-B	1000	6.09 ± 0.18	185 ± 10
	2000	5.98 ± 0.24	180 ± 14
$_{mono}$UiO-66-NH_2-30%-A	1000	4.80 ± 0.25	169 ± 16
	2000	4.58 ± 0.20	155 ±13

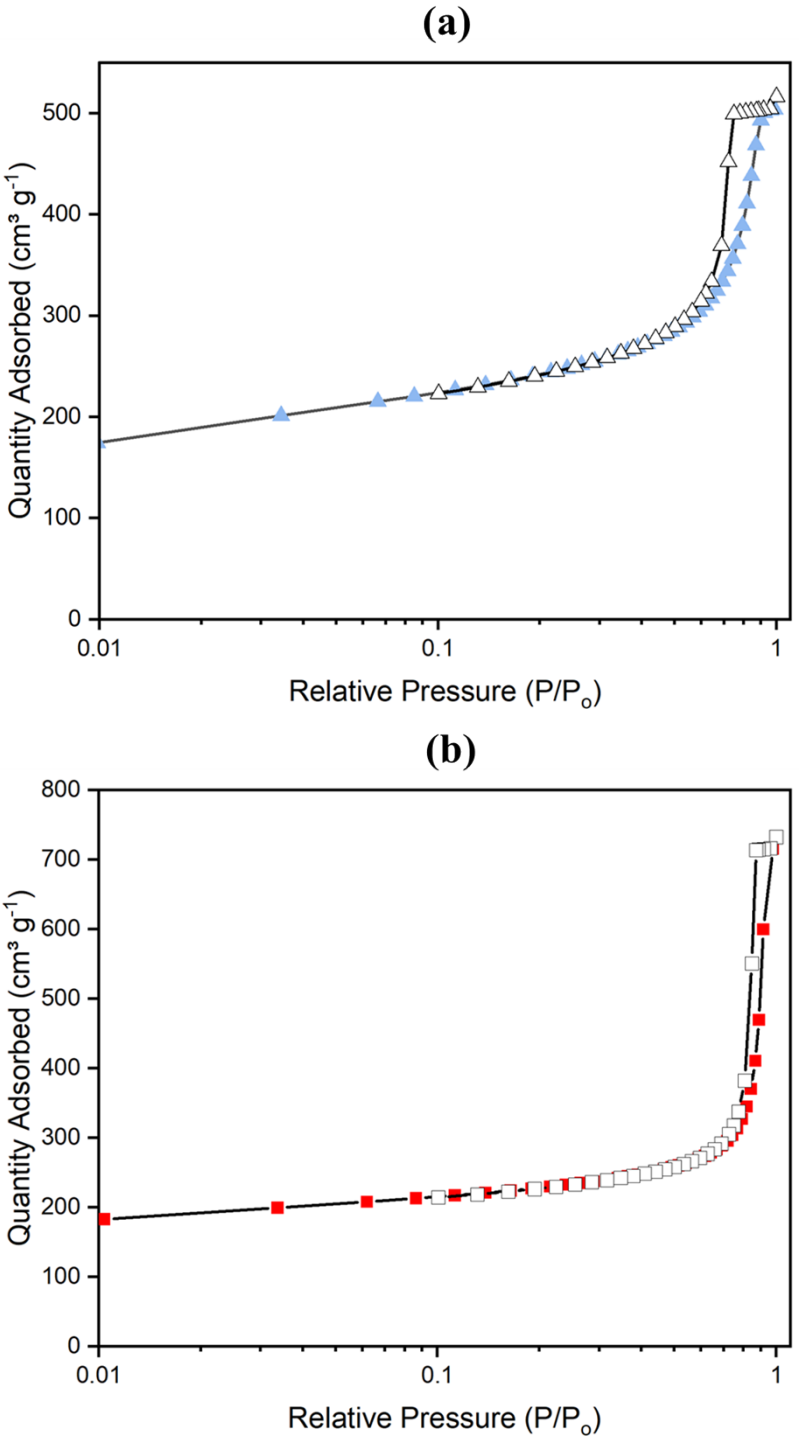

Figure S14: Low pressure N_2 gas adsorption data for isotherms measured at 77 K for (a) $_{mono}$UiO-66-NH_2-30%-B (solid triangles represent adsorption, and open triangles denote desorption); (b) $_{mono}$UiO-66-NH_2-30%-A (solid squares represent adsorption, and open squares denote desorption).

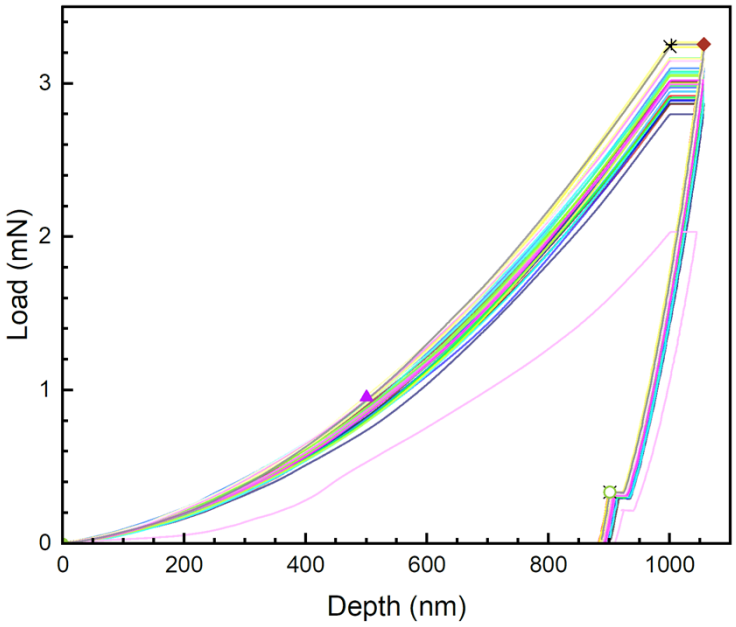

Figure S15: Load-displacement (*P-h*) nanoindentation data for $_{mono}$UiO-66-NH_2-30%-B. 2 sets of 16 indents were performed in different areas, setting the maximum indentation depth to 1000 nm. The highly reproducible *P-h* data reflect the homogeneity of the sample tested.

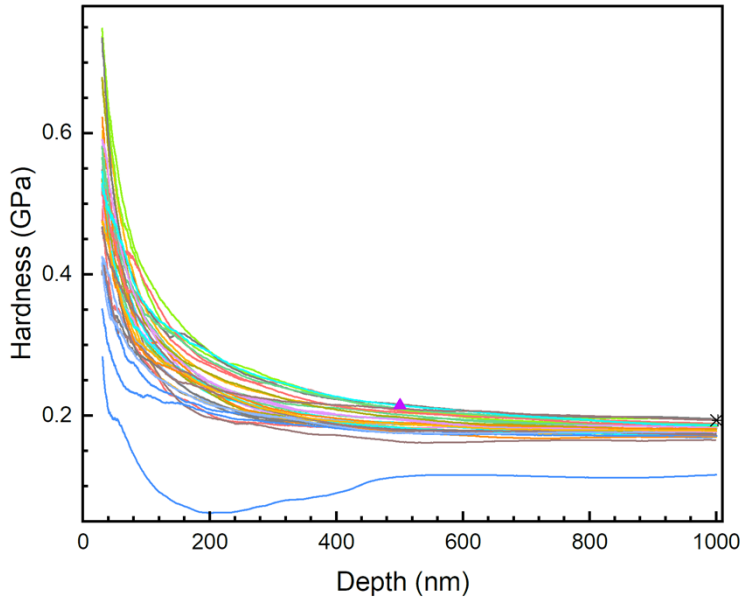

Figure S16: Hardness of $_{mono}$UiO-66-NH_2-30%-B plotted as a function of indentation depth. 2 sets of 16 indents were performed. Averaged hardness was determined using data collected over the 500-1000 nm indentation depth range, yielding 185 ± 10 MPa.

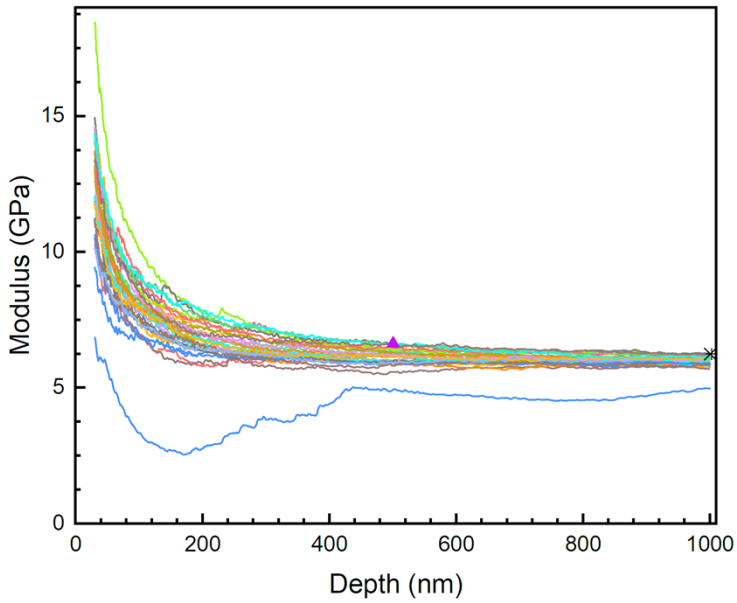

Figure S17: Indentation modulus, E^*, of $_{mono}$UiO-66-NH_2-30%-B plotted as a function of indentation depth. 2 sets of 16 indents were performed. Averaged indentation modulus was determined using data collected over the 500-1000 nm indentation depth range, yielding 6.09 ± 0.18 GPa.

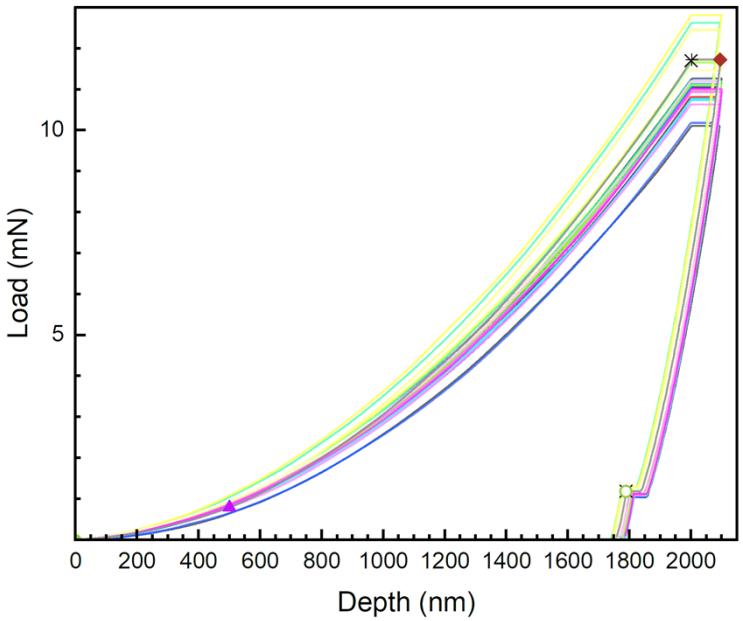

Figure S18: Load-displacement (*P-h*) nanoindentation data for $_{mono}$UiO-66-NH_2-30%-B. 2 sets of 16 indents were performed in different areas, setting the maximum indentation depth to 2000 nm. The highly reproducible *P-h* data reflect the homogeneity of the sample tested.

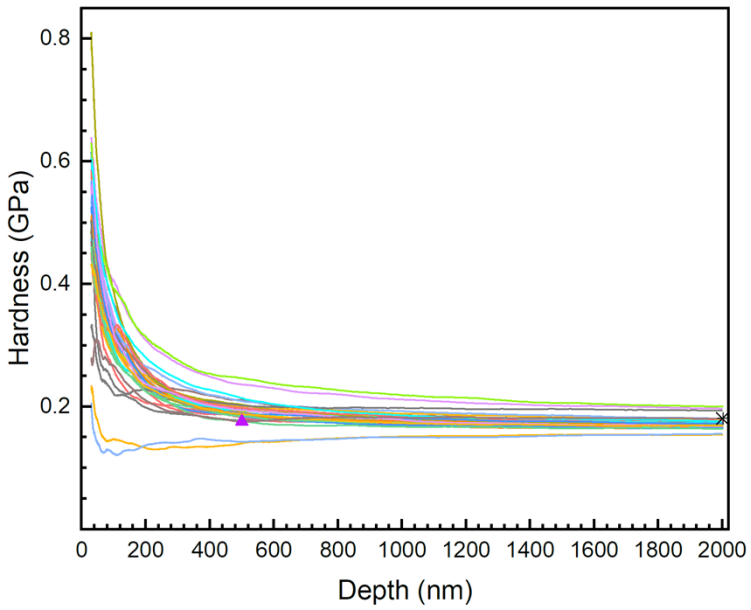

Figure S19: Hardness of $_{mono}$UiO-66-NH_2-30%-B plotted as a function of indentation depth. 2 sets of 16 indents were performed. Averaged hardness was determined using data collected over the 500-2000 nm indentation depth range, yielding 180 ± 14 MPa.

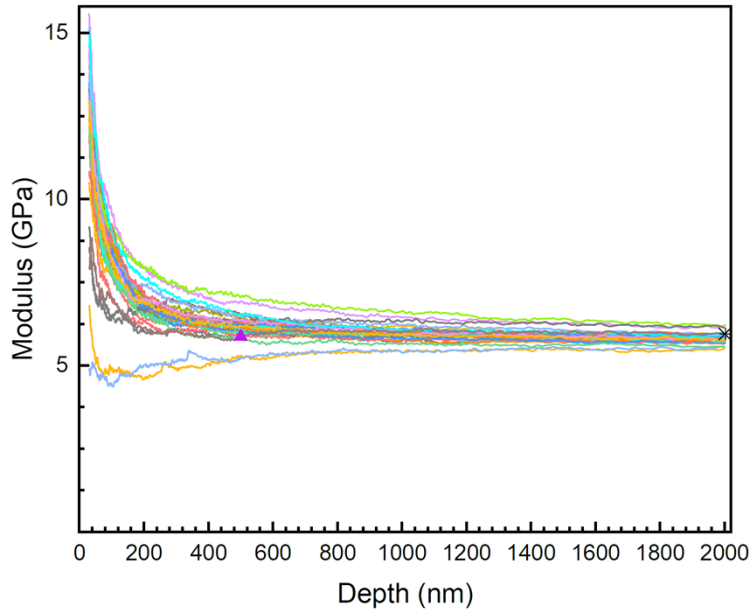

Figure S20: Indentation modulus, E^*, of $_{mono}$UiO-66-NH_2-30%-B plotted as a function of indentation depth. 2 sets of 16 indents were performed. Averaged indentation modulus was determined using data collected over the 500-2000 nm indentation depth range, yielding 5.98 ± 0.24 GPa.

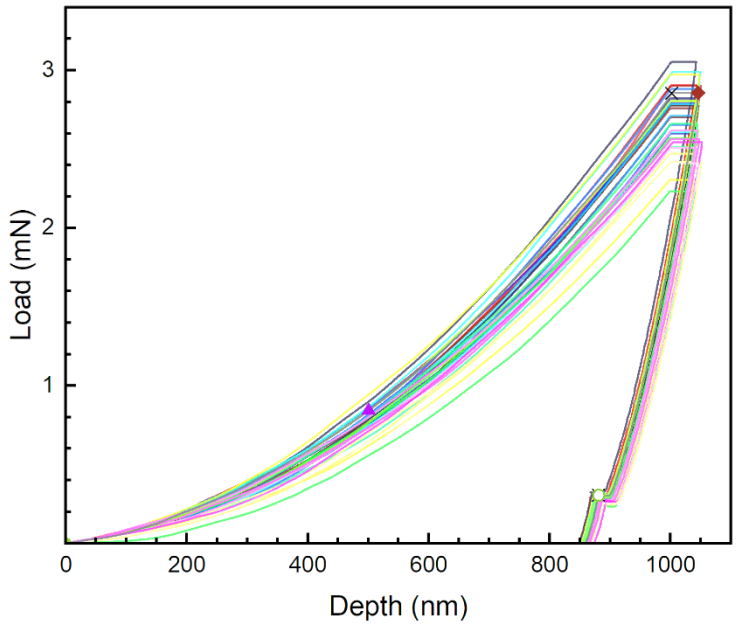

Figure S21: Load-displacement (*P-h*) nanoindentation data for $_{mono}$UiO-66-NH_2-30%-A. 2 sets of 16 indents were performed in different areas, setting the maximum indentation depth to 1000 nm. The highly reproducible *P-h* data reflect the homogeneity of the sample tested.

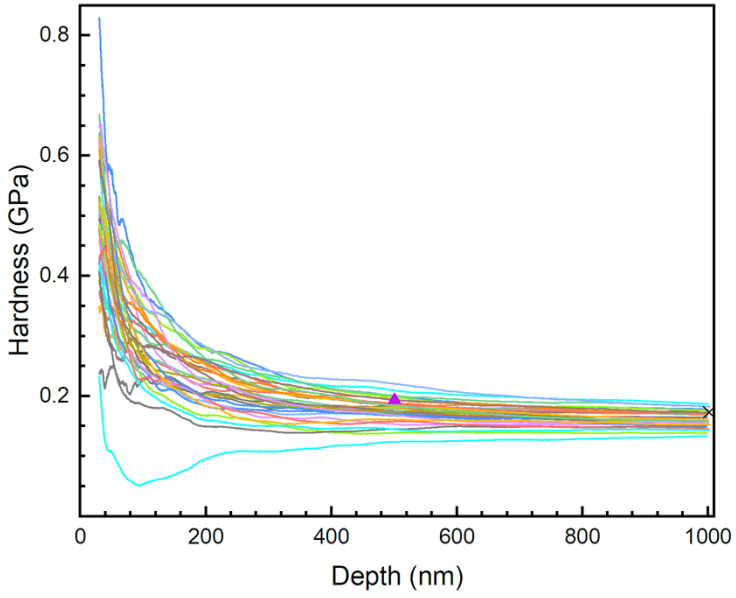

Figure S22: Hardness of $_{mono}$UiO-66-NH_2-30%-A plotted as a function of indentation depth. 2 sets of 16 indents were performed. Averaged hardness was determined using data collected over the 500-1000 nm indentation depth range, yielding 169 ± 16 MPa.

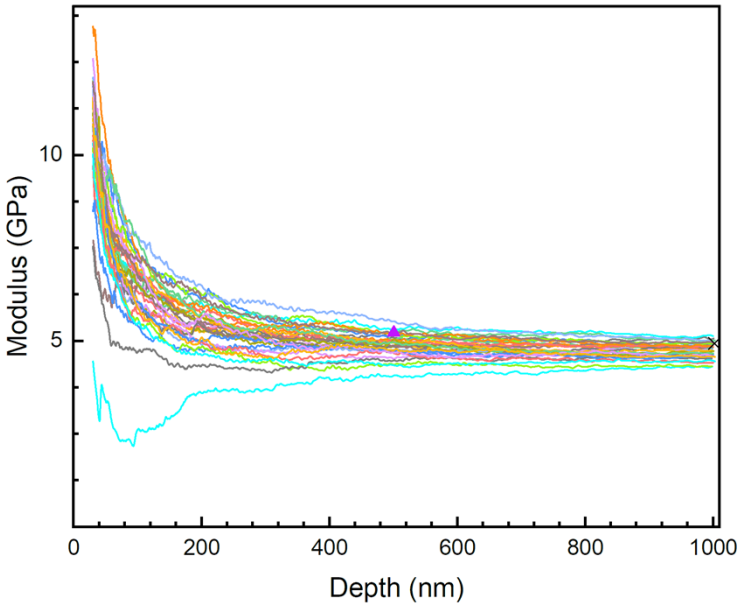

Figure S23: Indentation modulus, E^*, of $_{mono}$UiO-66-NH_2-30%-A plotted as a function of indentation depth. 2 sets of 16 indents were performed. Averaged indentation modulus was determined using data collected over the 500-1000 nm indentation depth range, yielding 4.80 ± 0.25 GPa.

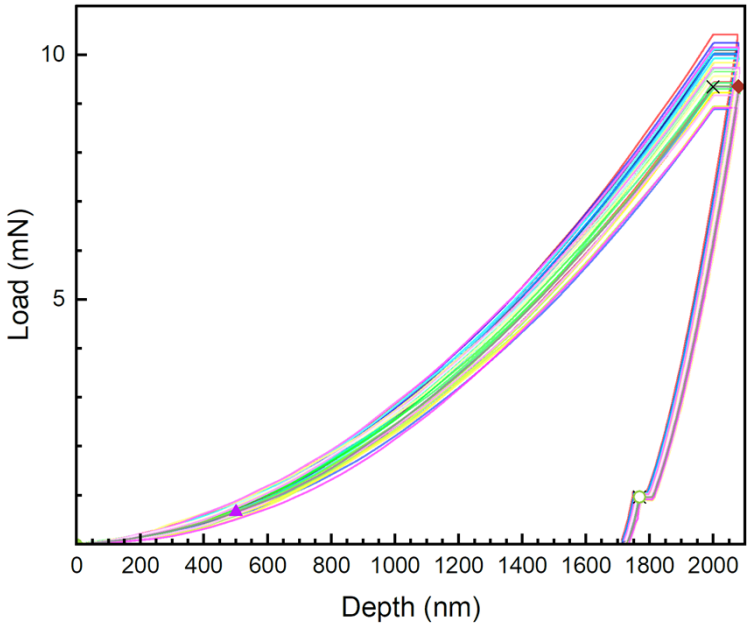

Figure S24: Load-displacement (*P-h*) nanoindentation data for $_{mono}$UiO-66-NH_2-30%-A. 2 sets of 16 indents were performed, setting the maximum indentation depth to 2000 nm. The highly reproducible *P-h* data reflect the homogeneity of the sample tested.

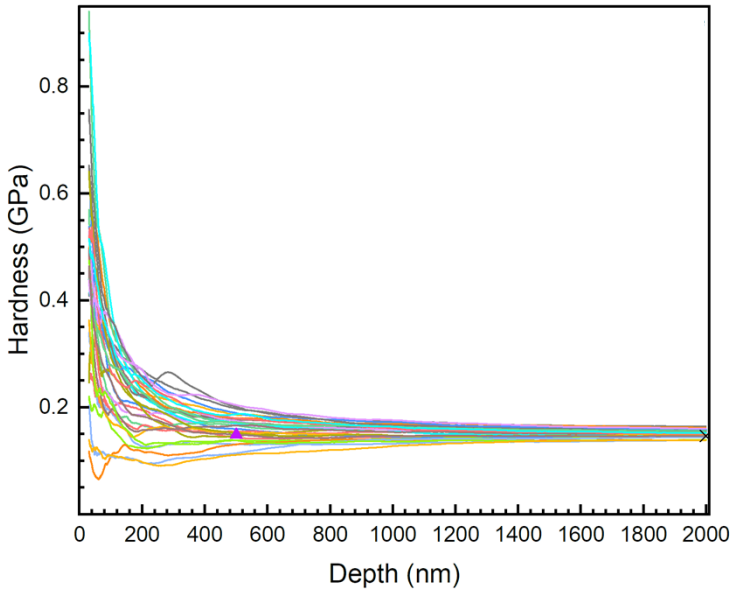

Figure S25: Hardness of $_{mono}$UiO-66-NH_2-30%-A plotted as a function of indentation depth. 2 sets of 16 indents were performed. Averaged hardness was determined using data collected over the 500-2000 nm indentation depth range, yielding 155 ± 13 MPa.

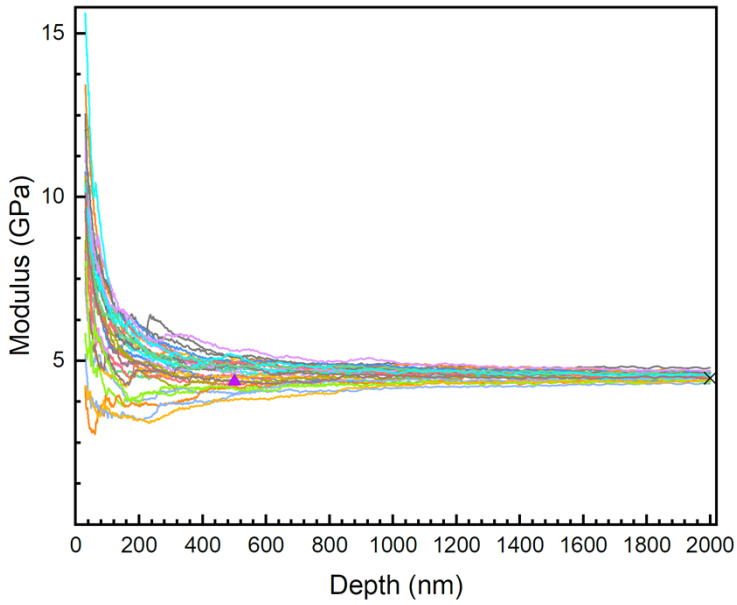

Figure S26: Indentation modulus, E^*, of $_{mono}$UiO-66-NH_2-30%-A plotted as a function of indentation depth. 2 sets of 16 indents were performed. Averaged indentation modulus was determined using data collected over the 500-2000 nm indentation depth range, yielding 4.58 ± 0.20 GPa.

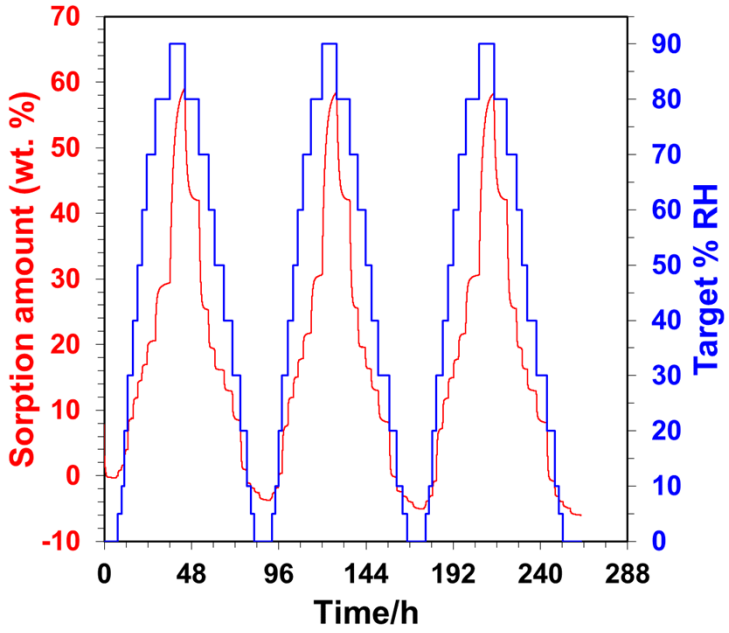

Figure S27: DVS water sorption kinetics over three isotherm cycles for $_{mono}$UiO-66-NH_2-30%-B using Intrinsic-DVS instrument at 27 °C. The sample was heated for 6 h at 40 °C and 0% RH between cycles.

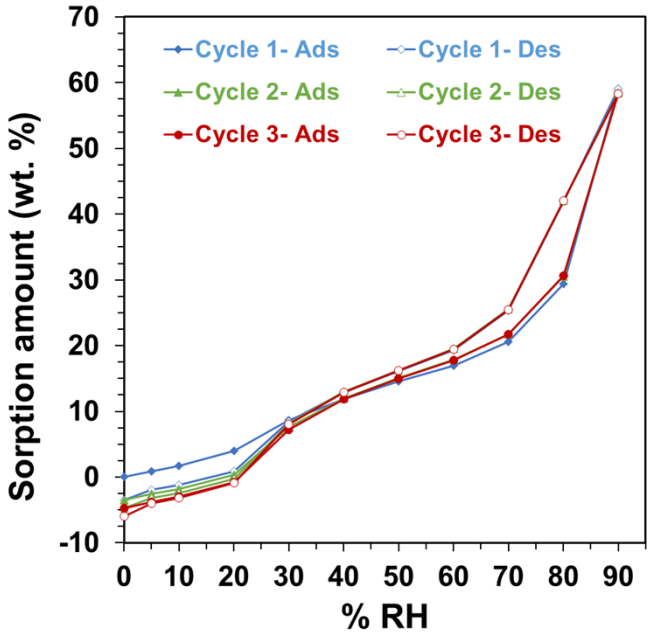

Figure S28: Triplicated DVS water sorption isotherms for $_{mono}$UiO-66-NH_2-30%-B using Intrinsic-DVS instrument at 27 °C. The sample was heated for 6 h at 40 °C and 0% RH between cycles.

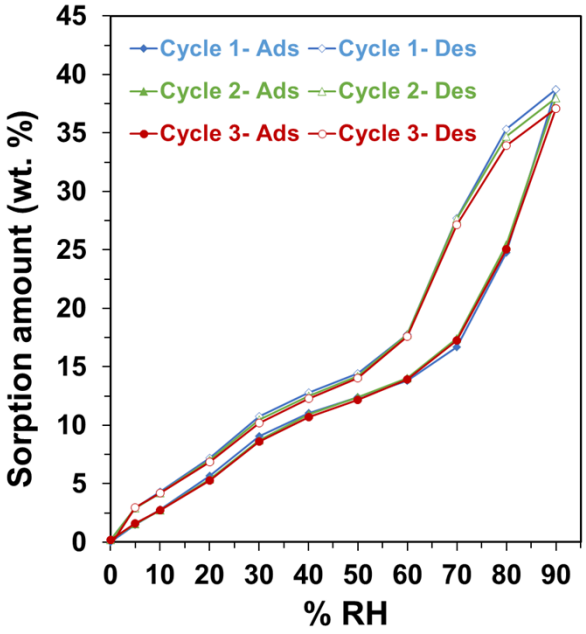

Figure S29: Triplicated DVS water sorption isotherms for $_{mono}$UiO-66-NH_2-30%-A at 27 °C. The sample was heated for 6 h at 40 °C and 0% RH between cycles.

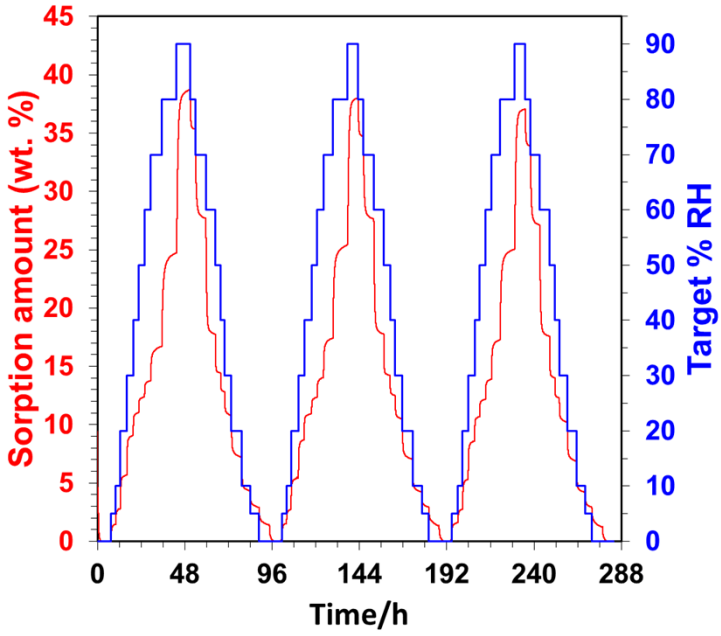

Figure S30: DVS water sorption kinetics over three isotherm cycles for $_{mono}$UiO-66-NH_2-30%-A at 27 °C. The sample was heated for 6 h at 40 °C and 0% RH between cycles.